https://dx.doi.org/10.1016/j.ijhydene.2021.11.022

Effects of cathode thickness and microstructural properties on the performance of Protonic Ceramic Fuel Cell (PCFC): a 3D modelling study

Zheng Li, Qijiao He, Lingchao Xia, Qidong Xu, Chun Cheng, Jian Wang, Meng Ni*

Department of Building and Real Estate, Research Institute for Sustainable Urban Development (RISUD) & Research Institute for Smart Energy (RISE), The Hong Kong Polytechnic University, Hung Hom, Kowloon, Hong Kong, China

* Corresponding author: Meng Ni
Email: meng.ni@polyu.edu.hk; Tel: 852-27664152

Abstract

Protonic Ceramic Fuel Cells (PCFCs) are promising power sources operating at an intermediate temperature. Although plenty of experimental studies focusing on novel material development are available, the design optimization of PCFC through numerical modelling is limited. In this study, a 3D PCFC model focusing on the cathode thickness and microstructure design is developed due to the high overpotential loss of the cathode. Unlike the 1D/2D models, the rib-size effects on the PCFC performance are fully considered when optimizing the cathode structure. Different from 1D/2D models suggesting thin cathode thickness, this study finds that the optimal cathode thickness is about 120-200 μm. In a thin cathode, weak O_2 diffusion from the channel to the rib-covered cathode can lead to O_2 depletion under the rib and very low local cell performance. By adjusting the cathode porosity from 0.3 to 0.5, nearly 9% performance improvement and 22.5% improvement in gas distribution uniformity can be achieved. When the cathode particle size changes from 0.1 μm to 0.2 μm, the O_2 concentration under the rib increases nearly 50%. The optimal electronic phase volume fraction is suggested to be around 50-60% for achieving a balance between ohmic resistance and reaction sites. This model elucidates the relationship between cathode microstructure and PCFC performance comprehensively and can serve as a guiding tool for cell fabrication and future novel interconnect structure design.

Keywords

Protonic ceramic fuel cell; numerical modelling; cathode microstructure; cathode thickness.

Nomenclature

Abbreviation

PCFC	Protonic ceramic fuel cell
SOFC	Solid oxide fuel cell
PEN	Positive electrode-electrolyte-negative electrode
TPB	Triple phase boundaries
ASR	Area-specific resistance, Ω m^2

Letter

E	Potential, V
R	Universal molar gas constant, 8.314 J mol^{-1} k^{-1}
T	Temperature, K
F	Faraday constant, 96485.33 C mol^{-1}
P_i^{TPB}	The partial pressure of species of i, Pa
i	Current density, A m^{-2}
I	Current, A
α	Charge transfer coefficient
n	Transferred electrons in the reaction
η	Overpotential, V
γ	Pre-factor
ϕ	Potential, V
λ_{TPB}^V	TPB length per volume, m m^{-3}
λ_{TPB}^A	TPB length per surface, m m^{-2}
P_k	Percolation probability of k phase particles
σ	Conductivity, S/m

ε	Porosity
ζ	Bruggeman factor
$Z_{k,k}$	Average number of contacts between k particles
ϕ_k	Volume fraction of k particle
r_k	Particle-radius of k particle
Z	Average total coordinate number, 6
n_{ele}^{V}	Number density of electronic particles
θ	Contact angle between particles, 30°
$\boldsymbol{N}_i$	Molar flux of species i
D_{iK}^{eff}	Effective Knudsen diffusion coefficient of species i, m^2/s
D_{ij}^{eff}	Effective binary diffusion coefficient, m^2/s
τ	Tortuosity
y_j	Molar fraction of the species i
μ	Viscosity, Pa s
k	Permeability, m^2
M_i	Molar mass of species i
r_p	Mean pore radius, m
ρ	Density, kg m^{-3}
$\boldsymbol{u}$	Velocity, m s^{-1}
$\boldsymbol{I}$	Unit matrix
C_p	Thermal capacity, J mol- k-1
k	Thermal conductivity, W m^{-1} k^{-1}
S	Entropy, J K^{-1} kg^{-1}
Q	Source term

Γ	Gas flow uniformity indicator
$\bar{c}$	Averaged mean concentration, mol m^{-3}
c_i	Concentration of species i, mol m^{-3}

Subscript

act	Activation
an, ca	Anode and cathode
conc	Concentration
Eq	Equilibrium
pro, ele	Protonic and electronic
eff	Effective

1. Introduction

In recent years, many countries and regions have proposed their ambitious goals in response to severe climate change and energy crises. For example, the Chinese government announced to achieve carbon neutrality progressively up to 2060, while the European Commission passed a series of legislation for achieving carbon neutrality by 2050 [1,2]. Therefore, great efforts should be made to revolutionalize the existing energy structure, that is, to reduce dependence on traditional fossil fuels and increase the share of clean and sustainable energy. As an energy conversion device that directly converts chemical energy into electric power, solid oxide fuel cells (SOFCs) have drawn much attention owing to their low carbon emission and higher conversion efficiency than conventional thermal power plants [3]. In addition, compared to other alternative fuel cells, SOFCs exhibit several advantages such as fuel flexibility, solid electrolyte, use of non-noble metal catalyst, fast electrochemical reaction kinetics[4–6]. However, the conventional SOFC based on oxygen-ion (O^{2-}) conducting electrolyte (shown in

Figure 1 (a)) needs high operating temperature (800-1000 °C) to attain sufficiently high oxygen ion conductivity which places high requirements on components materials [7]. For example, components materials should have similar thermal expansion coefficients for minimizing thermal stress and show splendid thermal and mechanical stability during the long time high-temperature operation [8,9]. PCFC (shown in Figure 1 (b)) is a promising alternative since it allows operation at intermediate temperature (400-700 °C), which leads to a increase in both fuel cell voltage and theoretical efficiency [10–12]. Unlike the counterpart SOFC, during the PCFC operation, H_2O is generated at the cathode side, enabling 100% fuel utilization. Thus, in the anode of PCFC, low concentration overpotential and high Nernst potential can be achieved. Both SOFC and PCFC are all-solid-state fuel cells operating above 400 °C. Other fuel cell technologies either cannot reach such high temperatures such as phosphoric acid fuel cell and proton exchange membrane fuel cell or are not all solid-state such as molten carbonate fuel cell [13,14]. Based on the cell structure and working temperature, it is more reasonable to compare PCFC with SOFC.

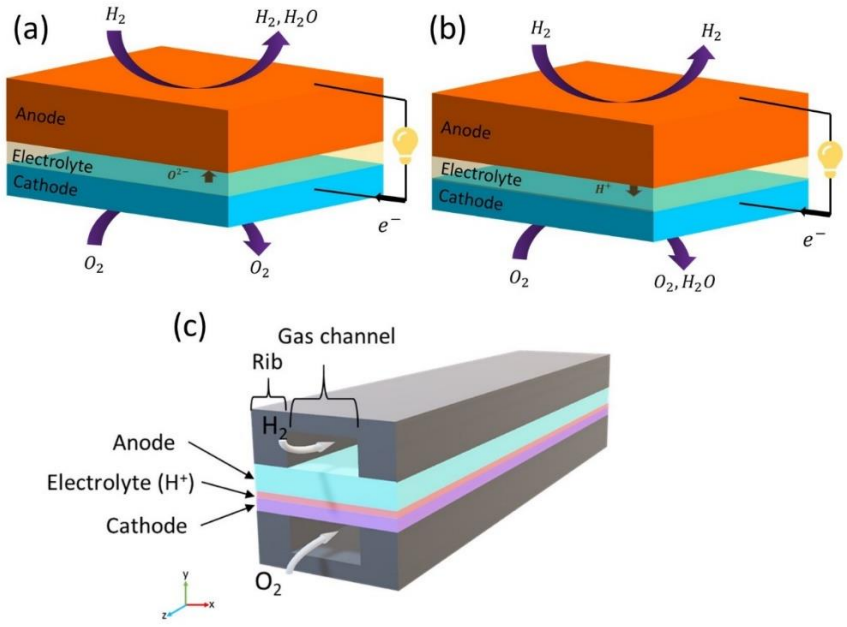

Figure 1 Schematic diagrams of (a) SOFC and (b) PCFC (c) 3D schematic of a PCFC stack cell [15].

Most of the recent experimental studies on PCFC are mainly based on anode-support PCFC. A thin electrolyte (10-20 μm) is often adopted for reducing the ohmic overpotentials, and a thin cathode (20-40 μm) layer is used for achieving low concentration losses [16–20]. However, as shown in Figure 1 (c), a PCFC stack cell composes of the PEN assembly (positive electrode/electrolyte/negative electrode) and interconnects. The presence of the interconnect ribs tends to cause non-uniform gas distribution within the thin cathode. In addition, the widths of the channel and the rib are significantly larger than their heights. As a consequence, the transport paths for electric current, as well as mass transport in the x-axis, can be much greater than those in the y-axis, which may result in high ohmic overpotential and concentration loss.

Several previous modelling studies investigate the performance of SOFC cathode in the presence of interconnects. Geisler et al. [21] found that both gas transfer and electrical current conduction in a thin cathode were significantly limited by ribs. Their results showed that increasing the concentration in the gas channel and entire cathode was necessary to maintain the stack cell performance. Jeon et al. [22] revealed that the large in-plane ohmic losses could give rise to a huge variation in the electric voltage in the cathode. The smaller pitch width (rib width + channel width) and larger rib ratio (rib width/pitch width) were found to be favorable to enhance the gas transport in the cathode and reduce the contact resistance. Liu et al. [23] showed that, at the same rib ratio, the oxygen depletion region underneath the rib was more obvious due to the larger rib width. They also found that oxygen depletion can lead to high concentration losses in the cathode. Su et al. [24] built a 2D model to investigate the effects of cathode thickness on SOFC performance. They concluded that the ohmic losses were decreased in a thicker cathode, and the O_2 distribution was promoted. Additionally, several studies focusing on PCFC cathode have been reported as well. Zhang et al. reported a $Ba_{0.5}Sr_{0.5}Sc_{0.175}Nb_{0.025}Co_{0.8}O_{3-\delta}$ cathode [25]. They found that the decrease in cathode performance can be attributed to the lack of active sites due to the agglomeration of cathode

particles and the coverage of the generated water. Xia et al. developed a $BaFe_{0.5}Sn_{0.2}Bi_{0.3}O_{3-\delta}$ cathode for PCFC operation [26]. They found that the oxygen reduction in the cathode was strongly enhanced by Bi-doping perovskite. Xie et al. tested a double perovskite $Ba_{0.75}Ca_{0.25}Co_{1.5}$ $Fe_{0.4}Ni_{0.1}NdO_{5+\delta}$ as the cathode in a PCFC [27]. From their analysis of the oxygen reaction process in the cathode, the cell performance can be improved by enhancing the oxygen reduction and diffusion within the cathode. Yang et al. varied the content of carbon microspheres (pore former) to control the porosity of the electrode [28]. They found that the highest cell performance is obtained when the electrode presents a high porosity (approximately 0.4). Lai and coworkers applied polystyrene nanospheres as pore former [29]. A $La_{0.6}Sr_{0.4}Co_{0.2}Fe_{0.8}$ $O_{3-\delta}$ cathode with graded porosity was developed. It was found that the cathode with a graded porosity structure can enhance the PCFC performance by reducing the ohmic and activation losses.

To the authors' best knowledge, though the effects of cathode thickness, rib widths and rib ratios on the performance of SOFC have been studied, their effects are usually analysed separately. For example, when studying the thickness effect, the rib effect on the optimal thickness is not considered. When analysing the rib width effect, it is usually done for a cross-section of SOFC without fully considering the variation of physical parameters along the flow channels. No modelling study at cell-level has been reported to explore the impacts of cathode thickness and cathode microstructural properties on the PCFC performance.

In order to fill in this research gap, a comprehensive three-dimensional model adopting percolation theory is constructed in the present study. The electrochemistry, charged species transport, mass/momentum transport are taken into account. In addition, the previous SOFC modelling study that investigated the effects of interconnects and cathode thickness did not consider heat transfer, but it is fully considered in this study. The heat transfer sub-model helps to analyze the temperature distribution in the cell and makes the simulation more realistic. This

model tries to provide an elucidation for the complex interrelationship between the cathode characteristics and PCFC performance. Herein, an optimal cathode thickness range for PCFC operation is proposed. It is also worthy to note that a special focus on the cathode zone underneath the rib is provided by this research work. This model can be used as a powerful tool to guide the manufacture of PCFC cathode and the design of the novel interconnect structure.

2. Modelling Methodology

2.1 Model geometry and assumptions

A 3D model for an anode-support PCFC is developed in this study. The computational domain includes two interconnects at the anode/cathode sides, two flow channels at the anode/cathode sides and the PEN assembly. The geometry input of the PCFC model is collected in Table 1.

Table 1 Geometrical parameters for PCFC [30].

Cell components	**Value**	**Units**
Cell length	30	mm
Cell width	2	mm
Gas channel height	0.5	mm
Gas channel width	1	mm
Interconnect thickness	0.65	mm
Anode support layer thickness	485	μm
Anode active layer thickness	15	μm
Electrolyte thickness	20	μm
Cathode active layer thickness	15	μm
Cathode support layer thickness	25	μm

The main assumptions adopted in this numerical model are listed below:

1) All the gas species (H_2, O_2, N_2, H_2O) are assumed to be ideal gases and they transport

as laminar flow in the gas channels.

2) The model simulates the PCFC operation at a steady state.
3) Both electronic and protonic phases are assumed to be evenly distributed in the anode and cathode.
4) Both electronic and protonic particles are assumed to have the same particle radius.

2.2 Electrochemical model

As mentioned before, the electrolyte in the PCFC conducts protons instead of oxygen ions. Thereby, two half electrochemical reactions at the anodic and cathodic sides should be written as:

$$Anodic\ side: 2H^+ + 2e^- \rightarrow H_2 \tag{1}$$

$$Cathodic\ side: 1/2O_2 + 2H^+ + 2e^- \rightarrow H_2O \tag{2}$$

The equilibrium potential of the electrochemical reaction is described by the Nernst equation [31].

$$E_{eq} = 1.2535 - 0.00024516 \times T + \frac{RT}{2F} ln\left(\frac{P_{H_2}^{TPB}\left(P_{O_2}^{TPB}\right)^{0.5}}{P_{H_2O}^{TPB}}\right) \tag{3}$$

Where P_i^{TPB} is the partial pressure of each gas species at the triple phase boundaries (TPBs). Thereupon, the concentration overpotentials (η_{conc}) of PCFC are implicitly taken into account. The Butler-Volmer equations are employed to calculate the current densities at the anodic (i_{an}) and cathodic sides (i_{cn}), respectively.

$$i_{an} = i_{0,an}\left(exp\left(\frac{\alpha_{an} nF\eta_{act,an}}{RT}\right) - exp\left(\frac{-(1-\alpha_{an})nF\eta_{act,an}}{RT}\right)\right) \tag{4}$$

$$i_{ca} = i_{0,ca}\left(exp\left(\frac{\alpha_{ca} nF\eta_{act,ca}}{RT}\right) - exp\left(\frac{-(1-\alpha_{ca})nF\eta_{act,ca}}{RT}\right)\right) \tag{5}$$

Where α_{an} and α_{ca} are the anodic and cathodic asymmetric charge transfer coefficients

respectively, $\eta_{act,an}$ and $\eta_{act,ca}$ denote the anodic and cathodic activation losses respectively, $i_{0,an}$ and $i_{0,ca}$ represent the anodic and cathodic exchange current densities respectively, which can be furthered defined as [32,33]:

$$i_{0,an} = \gamma_{an} \frac{RT}{nF} \left(P_{H_2}^{TPB}\right)^b exp\left(-E_{act,an}/RT\right) \tag{6}$$

$$i_{0,ca} = \gamma_{ca} \frac{RT}{nF} \left(P_{O_2}^{TPB}\right)^c \left(P_{H_2O}^{TPB}\right)^d exp\left(-E_{act,ca}/RT\right) \tag{7}$$

Where γ_{an} and γ_{ca} are the pre-factors for the anode and cathode respectively, $E_{act,an}$ and $E_{act,ca}$ denotes the activation energies for the anodic and cathodic reactions respectively, b, c, and d are the orders of partial pressure. Noteworthy, γ_{an}, γ_{ca}, b, c, and d are obtained by fitting the experimental data.

Besides, the working potential of the PCFC cell, V, can be expressed as:

$$V = E_{eq} - \eta_{act,an} - \eta_{act,ca} - \eta_{ohmic,an} - \eta_{ohmic,ca} - \eta_{ohmic,ele} - \eta_{ASR,an} - \eta_{ASR,ca} \tag{8}$$

Where $\eta_{ohmic,an}$, $\eta_{ohmic,ca}$ and $\eta_{ohmic,ele}$ are the ohmic losses of the anode, cathode and electrolyte, respectively, $\eta_{ASR,an}$ and $\eta_{ASR,ca}$ are the potential losses caused by contact resistances at the anode-interconnect and cathode interconnect interfaces respectively.

2.3 Charge transport

Both protonic and electronic transport follow Ohm's law associated with the charge continuity equations [34].

$$\nabla \cdot \boldsymbol{i}_{pro} = \nabla \cdot \left(-\sigma_{pro,eff} \nabla \phi_{pro}\right) = -i_0 \lambda_{TPB}^V \tag{9}$$

$$\nabla \cdot \boldsymbol{i}_{ele} = \nabla \cdot \left(-\sigma_{ele,eff} \nabla \phi_{ele}\right) = i_0 \lambda_{TPB}^V \tag{10}$$

Where $\boldsymbol{i}_{pro}$ and $\boldsymbol{i}_{ele}$ are the protonic and electronic current vectors respectively, $\sigma_{pro,eff}$ and $\sigma_{ele,eff}$ are the effective conductivities for the protonic and electronic transports in the PCFC

respectively. It is worth to noting that the proton conduction is a significant performance-limiting factor in the porous cathode due to the relatively low protonic conductivity, compared with electrical conductivity. Therefore, the ion conduction only occurs in a thin layer near the cathode-electrolyte interface [35]. In this study, when we change the cathode thickness in the presence of the rib, the change in proton conduction is negligible compared with more significant change in electron conduction. Hence, we focus on the effects of cathode thickness on the electron transfer instead of proton transfer in this research. In this model, the percolation theory is incorporated to unveil the relationship between electrode microstructural properties and the effective electrode properties. Detailed information concerning the percolation theory can be found in refs. [36,37]. Thus, based on percolation theory, the effective conductivity k (k=protonic or electronic) phase can be determined as [6]:

$$\sigma_{k,eff} = \sigma_{0,k}[(1-\varepsilon)\phi_k P_k]^{\zeta} \tag{11}$$

Where $\sigma_{0,k}$ is the intrinsic conductivity of the k phase material, ε is the porosity, ϕ_k is the volume fraction of the k phase particles, ζ is Bruggeman factor, which typically varies from 1.5-3 in the literature, P_k is the percolation probability for k phase particles, which can be estimated as [38,39]

$$P_k = 1 - [(\frac{4.236 - Z_{k,k}}{2.472})^{2.5}]^{0.4} \tag{12}$$

Where $Z_{k,k}$ is the average number of contacts between k particles, which can be determined by volume fraction (ϕ_k) and particle-radius (r_k) [36,37,40]:

$$Z_{pro,pro} = Z\frac{\phi_{ele}/r_{ele}}{\phi_{ele}/r_{ele} + \phi_{pro}/r_{pro}} \tag{13}$$

$$Z_{ele,ele} = Z\frac{\phi_{pro}/r_{pro}}{\phi_{pro}/r_{pro} + \phi_{ele}/r_{ele}} \tag{14}$$

Where Z is the average total coordinate number and is assigned to be 6 in a random packing

spheres system [37]. In this study, the ratio of electronic particle-radii to the protonic particle ratio is set to be 1.

In addition, the last term in the Eq.(9) and Eq. (10), λ_{TPB}^{V}, represents the TPB length per unit volume (m/m^3). TPBs are generated by the contact between percolated protonic particles, percolated electronic particles and the pore phases. Thus, the following equation can be applied to determine the λ_{TPB}^{V} [36,37]

$$\lambda_{TPB}^{V} = 2\pi min\left(r_{ele}, r_{pro}\right) P_{ele} P_{pro} n_{ele}^{V} Z_{ele,pro} sin(\theta/2) \tag{15}$$

Where θ, assumed to be 30°, is the contact angle between different particles, n_{ele}^{V} is the number density of electronic particles (no./m^3), namely, $n_{ele}^{V} = \left((1-\epsilon)\phi_{ele}\right)/(4\pi r_{ele}^{3}/3)$, $Z_{ele,pro}$ is the average number of contacts between an electronic particle and a protonic particle [41]. $Z_{ele,pro}$ may be determined by the following formula [37]

$$Z_{ele,pro} = \frac{Z}{2}\left(1 + \frac{r_{ele}^{2}}{r_{pro}^{2}}\right)\frac{\phi_{pro}/r_{pro}}{\phi_{ele}/r_{ele} + \phi_{pro}/r_{pro}} \tag{16}$$

Furthermore, TPBs can also be formed by the contact between the percolated electronic particles with the electrolyte surface. This area-specific TPB length (λ_{TPB}^{A}) can be expressed as follows [37]

$$\lambda_{TPB}^{A} = 4\pi r_{ele}^{2} P_{ele} n_{ele}^{V} sin(\theta/2) \tag{17}$$

2.4 Mass and momentum transport

The transport of gas species within the porous media consists of two diffusion phenomena, i.e., molecular diffusion and Knudsen diffusion. In the present work, the dust gas model is implemented to provide an accurate description of mass transport in the porous electrode. The molar flux of species i, $\boldsymbol{N}_i$, can be calculated as [42]

$$\frac{\boldsymbol{N}_i}{D_{iK}^{eff}} + \sum_{j=1}^{n} \frac{y_j \boldsymbol{N}_i - y_i \boldsymbol{N}_j}{D_{ij}^{eff}} = -\frac{1}{RT}\left(P\nabla y_i + y_i \nabla P + y_i \nabla P \frac{kP}{D_{iK}^{eff}\mu}\right) \tag{18}$$

Where y_i represents the mole fraction of the species i, P is the operating pressure, κ is the permeability, μ is the viscosity of species, D_{iK}^{eff} and D_{ij}^{eff} are the effective Knudsen diffusion coefficient of species i and the effective binary diffusion coefficient, respectively. These two kinds of diffusion coefficients can be expressed as [6,43–45]:

$$D_{ij}^{eff} = \frac{\varepsilon}{\tau} \frac{3.198 \times 10^{-8} T^{1.75}}{P\left(v_i^{1/3} + v_j^{1/3}\right)^2} \left(\frac{1}{M_i} + \frac{1}{M_j}\right)^{0.5} \tag{19}$$

$$D_{iK}^{eff} = \frac{\varepsilon}{\tau} \frac{2}{3} r_p \sqrt{\frac{8RT}{\pi M_i}} \tag{20}$$

$$r_p = \frac{2}{3}\left(\frac{\varepsilon}{1-\varepsilon}\right) \frac{1}{\phi_{ele}/r_{ele} + \phi_{pro}/r_{pro}} \tag{21}$$

Where τ is the tortuosity, M_i denotes the molar mass of species i, v_i represents the diffusion volume for species i, r_p signifies the mean pore radius.

In the gas channel, the momentum transport of gas flow can be described by the classic Navier-Stokes equation (Eq. (22), while the momentum transport of gas species in the porous electrode is governed by the Brinkman equation (Eq. (23) [46].

$$\rho(\boldsymbol{u} \cdot \nabla) \cdot \boldsymbol{u} = -\nabla P + \nabla \cdot [\mu(\nabla \boldsymbol{u} + \nabla \boldsymbol{u}^T)] \tag{22}$$

$$\frac{1}{\varepsilon}\rho(\boldsymbol{u} \cdot \nabla) \cdot \boldsymbol{u}\frac{1}{\varepsilon} = -\nabla P + \nabla \cdot \left[\mu \frac{1}{\varepsilon}(\nabla \boldsymbol{u} + \nabla \boldsymbol{u}^T) - \frac{2}{3}\mu \frac{\boldsymbol{I}}{\varepsilon}(\nabla \cdot \boldsymbol{u})\right] - \left(\mu \kappa^{-1} + \frac{Q_m}{\varepsilon^2}\right)\boldsymbol{u} \tag{23}$$

Where $\boldsymbol{u}$ is the velocity vector, ρ is the density, $\boldsymbol{I}$ is the unit matrix, Q_m is the source or sink term of mass.

2.5 Heat transport

The heat transport in the PCFC is a complex process involving the heat generation from electrochemical reactions (entropy change and the activation loss), ohmic loss and area-specific contact resistance ($ASR_{contact}$). In this study, heat convection and heat conduction are taken into consideration while the heat radiation is omitted owing to the small cell dimension. However, for large cell/stack modelling, it is suggested to consider the radiation effect for more accurate simulation. Hence, the energy conservation equation can be written as [32]:

$$\rho C_p \boldsymbol{u} \nabla T + \nabla \cdot \left(-k_{eff} \nabla T\right) = Q_h \tag{24}$$

Where C_p is the heat capacity, k_{eff} is the effective thermal conductivity. These two properties can be defined as:

$$C_p = \sum_i y_i \cdot C_{p,i} \tag{25}$$

$$k_{eff} = \varepsilon \cdot k_g + (1 - \varepsilon) \cdot k_s \tag{26}$$

$$k_g = \sum_i y_i \cdot k_i \tag{27}$$

Where $C_{p,i}$ represents the specific heat of species i, k_s denotes the heat conductivity of solid phase, k_i is the thermal conductivity of gas species i [47]. What noteworthy is that the thermodynamics and transport properties of different gas species as well as the thermal properties of solid materials adopted in this model can be found in the refs [48,49]. The remaining quantity in Eq. (24), Q_h , is the term of heat source or sink. For the electrochemical reactions, the heat generation can be calculated as:

$$Q_{elec} = (-T\Delta S) \cdot \frac{I}{nF} \tag{28}$$

Where ΔS is the net entropy change of the electrochemical reactions, I is the current. Additionally, the heat sources owing to ohmic overpotential and contact resistance may be

expressed as [50]:

$$Q_{ohmic} = -(i \cdot \nabla\phi) \tag{29}$$

$$Q_{cont} = Ai^2 ASR_{contact} \tag{30}$$

Where A is the contact area at the electrode-interconnect interface.

Table 2 Parameters adopted in the model [24,47,49]

Parameters	**Value or expression**	**Unit**
$E_{act,an}$	1.2×10^5	J/mol
$E_{act,ca}$	1.3×10^5	J/mol
γ_{an}	1.90×10^{10}	
γ_{ca}	1.80×10^{10}	
b	0.5	
c	1	
d	1	
σ_{Ni}	$9.5\times10^7 exp(-1150/T)/T$	S/m
σ_{BCZY}	$290.4exp(-4600.6/T)$	S/m
σ_{SSC}	$10^{(3.321183+1183/T-4.38\times10^5/T^2)}$	S/m
ε_{an}	0.3	
ε_{ca}	0.3	
τ	3	
$r_{ele,an}$	0.3	μm
$r_{ele,ca}$	0.3	μm

P_0	1	atm
T	973	K

2.6 Boundary conditions

The proper boundary conditions are significant to solve the governing equations of the model. The electric potential is set to zero at the anodic interconnect and to the operating potential at the cathodic interconnect. The contact resistance is set at the electrode-interconnect interfaces. The local current density across the interface can be solved by the potential changes across the interface ($\Delta\phi_{cross}$) associated with the contact resistance [23]:

$$i_{local} = \Delta\phi_{cross}/ASR_{contact} \quad (31)$$

All other boundaries and interfaces are electrically insulated. The boundary conditions of the gas inlet are set as 100 SCCM and 200 SCCM at anode gas channel and cathode gas channel, respectively. The no-slip condition is assigned to the walls for gas flow. At the anodic gas channel inlet, the molar composition of the gas is 97% H_2 with 3% H_2O while the air (79% N_2 with 21% O_2) is feed into the cathode gas channel. The mass transport boundary is arranged as insulation condition at the walls. The working temperature is selected as the inlet condition of the gas channels for the two electrodes. In addition to this, the two sides of the PCFC are set to symmetric conditions in the heat transfer sub-model.

2.7 Model validation

The present 3D model is numerically solved using the finite element method. The mesh independence is achieved with 260510 meshing elements. When the mesh is finer, the current density difference is less than 0.1%. The parameters and variables used in the present work are collected in Table 2. The model is validated by comparing the simulating data with the experimental data extracted from the literature [30,51,52]. The validation conditions are

consistent with the experimental conditions. A good agreement between the modelling results and experimental data is observed in Figure 2. Thus, the fidelity of this 3D model is considered verified. It can be employed for performing the subsequent series of parametric studies.

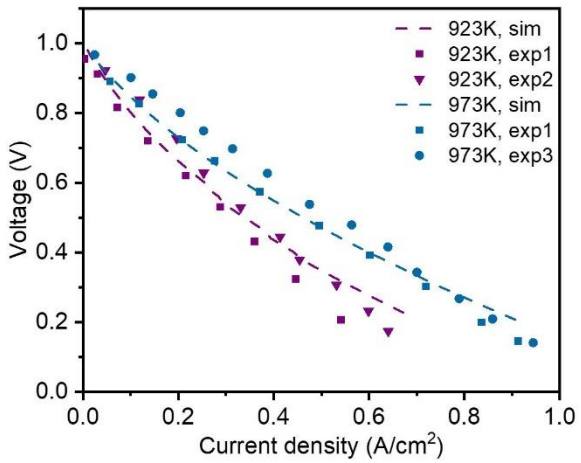

Figure 2 The comparison of modelling results and experimental results.

3. Results and discussion

3.1 Effects of cathode thickness

The effects of cathode thickness on the electrochemical performance of PCFC are investigated by adjusting the cathode thickness from 40 μm to 240 μm. Simulations are conducted at a given voltage of 0.7 V. The overall effect of the cathode thickness on the current density is shown in Figure 3 (a). The optimal cathode thickness is found to be 120 μm to produce the highest current density (at 973 K) and thus reach the highest energy efficiency (at 0.7 V). The resistance ($R=L/(A\sigma)$ is the ratio of the conductive length (L) to the product of the conductivity (σ) and the cross-section area (A). In the x-direction, the cross-sectional area increases with the increase of cathode thickness, and thus lead to the decrease in the ohmic overpotential. In the y-direction, the the conduction length decreases with the increase of cathode thickness, and thus lead to the increase in the ohmic overpotential. As mentioned before, the electron conduction pathway along the x-direction is much longer than that along the y-direction in the studied cathode thickness range, which leads to a huge difference between the ohmic loss along

the x-direction and the y-direction. As a result, the ohmic overpotential can be reduced by increasing the cathode thickness, which is also reported in the ref. [24]. It also illustrates that before the current density reaching the optimum, the magnitude of the slope of the current density growth is approximately equal to that of the ohmic polarization reduction. Thus, the change of current density is strongly sensitive to the ohmic loss reduction. The drop in current density can be attributed to the increase of concentration overpotential. In Figure 3 (b), the concentration loss in the x-direction and y-direction both increase with the increase of cathode thickness. Meanwhile, the concentration polarization under the rib area shows a gradual reduction since the rise in the x-directional cross-section area enhances the mass transport. It can be inferred that the increase of concentration loss comes from the cathode under the channel instead of the cathode under the rib.

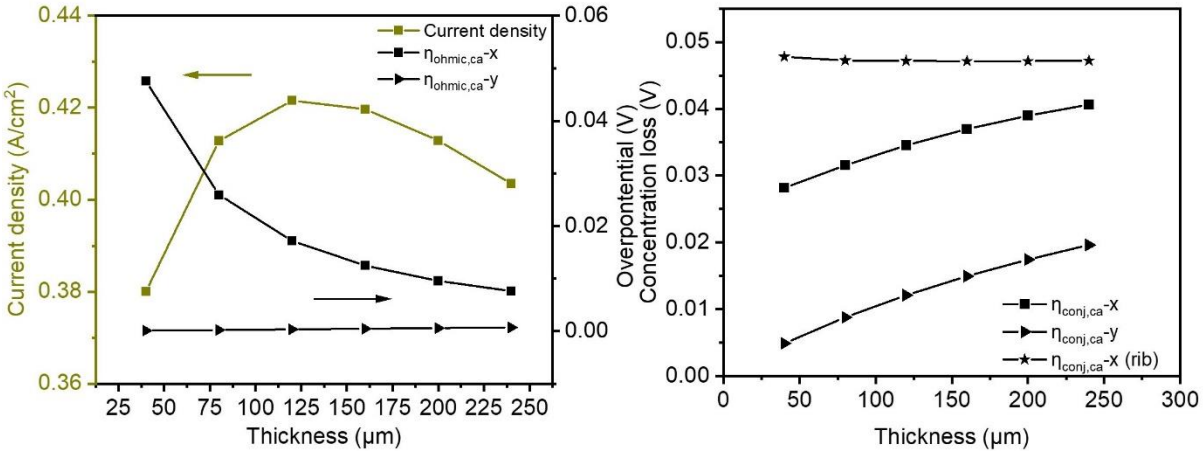

Figure 3 (a) Effects of cathode thickness on the current density and ohmic loss; (b) effects of cathode thickness on the concentration loss.

The impacts of cathode thickness on the gas flow distribution are examined in this section. A formula evaluating the gas distribution uniformity is adopted here [53]:

$$\Gamma = 1 - \left(\frac{\sum_{i=1}^{n}\left[\frac{(c_i - \bar{c})}{\bar{c}}\right]^2}{n}\right)^{0.5} \tag{32}$$

Where Γ is an indicator for describing the gas flow uniformity, n is the number of rib-channels

(in here n=1), $\bar{c}$ denotes the averaged mean concentration, c_i is the concentration of species i.

Figure 4 (a) denotes that the gas uniformity within the cathode is doubled when thickness changes from 40 μm to 240 μm. A more intuitive description is sketched in Figure 4 (b). The O_2 distribution within the cathode becomes more uniform and the O_2 concentration in the cathode area underneath the rib is improved. Therefore, the growth of the gas uniformity indicator can be mainly credited to the concentration enhancement in the cathode under the rib.

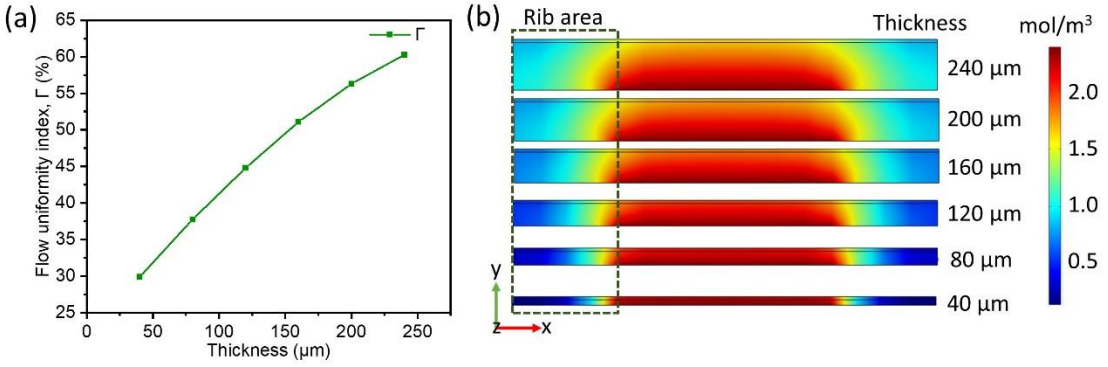

Figure 4 (a) The change of gas uniformity index in the cathode; (b) The distribution of the oxygen within the cathode (xy-plane).

In order to obtain a quantitative analysis of the effects of cathode thickness, the concentration and reaction rate of O_2 at the cathode-electrolyte interface along the x-direction are shown in Figure 5 (a) and (b), respectively. Increasing the cathode thickness tends to increase the O_2 concentration under the rib but tends to decrease the O_2 concentration under the channel. Due to a high O_2 concentration and low ohmic loss, the peak reaction rates are found under the channel-covered area except for t=40 μm. It should be noted that when t= 40 μm, about 50% of the cathode area under the rib exhibit almost zero O_2 concentration and reaction rate, which is consistent with results reported in Refs. [23,24]. This phenomenon indicates that the utilization efficiency of the cathode under the rib is relatively low with a thin cathode. Consequently, a thicker cathode can enhance the utilization of the cathode under the rib.

The drastic change of reaction rate within the rib-covered cathode zone may induce a large

temperature gradient in this region. The temperature difference in Figure 5 (c) shows a step profile due to the small dimension of PCFC. It also reveals that the temperature variation when t=40 μm is twice that when t=240 μm. The temperature gradient under the rib when t=40 μm is calculated as 8 K/cm which is smaller than the maximum temperature gradient (10 K/cm) suggested by literature [54]. In future work, a thermo-mechnical modelling study on PCFC can be performed to explore how the temperature gradient in the cathode contribute to the thermal stress.

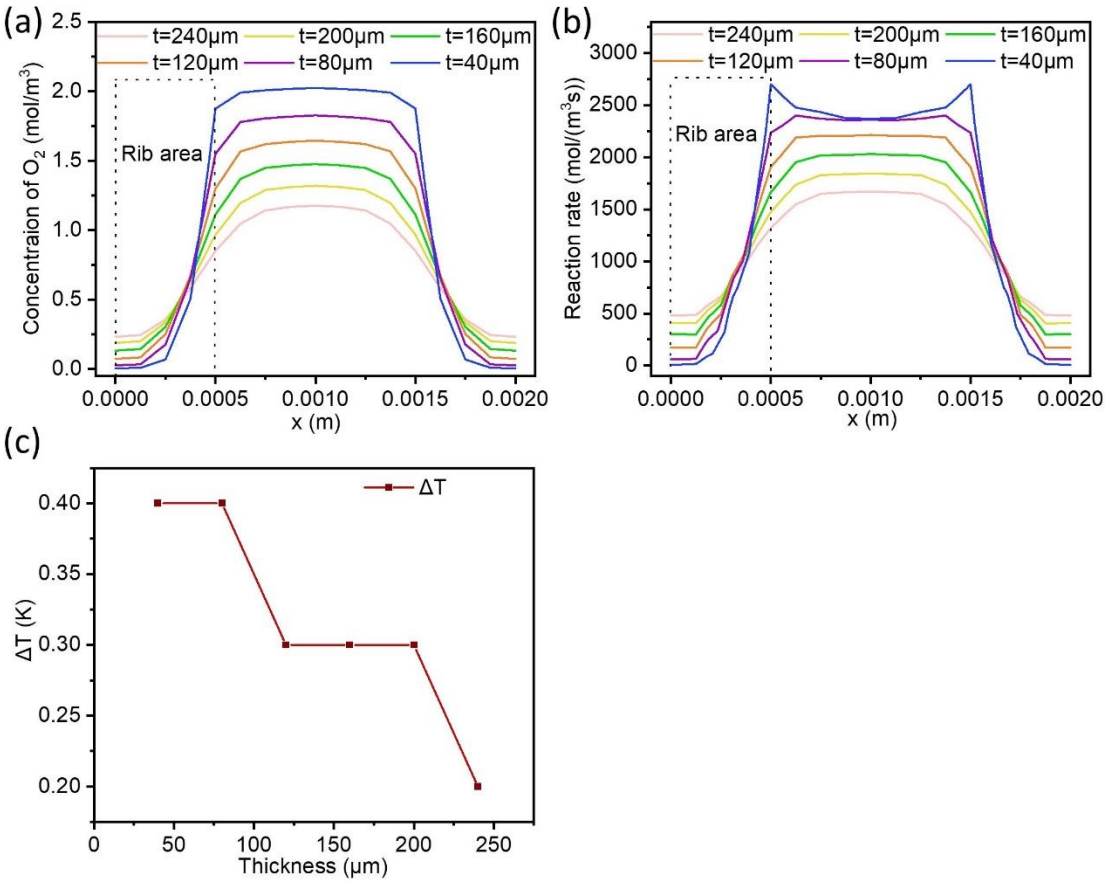

Figure 5 (a) The O_2 concentration distribution at cathode-electrolyte interface along the x-direction; (b) the O_2 reaction rate distribution at cathode-electrolyte interface along the x-direction; (c) the temperature variation that straddles the cathode region underneath the rib.

3.2 Effects of cathode porosity

Porosity plays a pivotal role in cathode performance. The effects of porosity are explored by varying the cathode porosity from 0.35 to 0.60. Figure 6 (a) illustrates that the optimal cathode

thickness is approximately from 120 μm to 200 μm under various porosities. Additionally, when the cathode thickness is fixed, it can be inferred that the current density rises as the porosity increases to 0.5 then decreases with a further increase in porosity from 0.5 to 0.6. The current density increase with increasing porosity is due to the reduction in concentration loss, while the reduction in current density when porosity adjusts from 0.5 to 0.6 can be ascribed to the increase in the ohmic loss. Hence, the optimal porosity is achieved by the trade-off of these two overpotentials. More details concerning this speculation will be provided and discussed later on. Figure 6 (a) shows that the optimal porosity for PCFC operation is between 0.45 and 0.5.

The O_2 concentration distribution shows a similar pattern in Fig. 6(b) and Fib. 5(a). However, with the increase of cathode thickness, the O_2 concentration in the cathode region under the rib at ε=0.5 is improved more significantly than that at ε=0.3. In the porous cathode under the channel, the difference in the O_2 concentration of various cathode thicknesses at ε=0.5 (approximately 0.1 mol/m^3) is less than that at ε=0.3 (approximately 0.25 mol/m^3). Besides, it can be found that the reaction rate under the rib is significantly augmented by comparing Figure 6 (c) with Figure 5 (b). The oxygen depletion area is eliminated at ε=0.5, thereby improving the utilization efficiency of the cathode zone underneath the rib. However, the reaction rate is weakened more conspicuously in the region under the channel when ε=0.5 than when ε=0.3, indicating the more significant impact of ohmic loss in this region when ε=0.5.

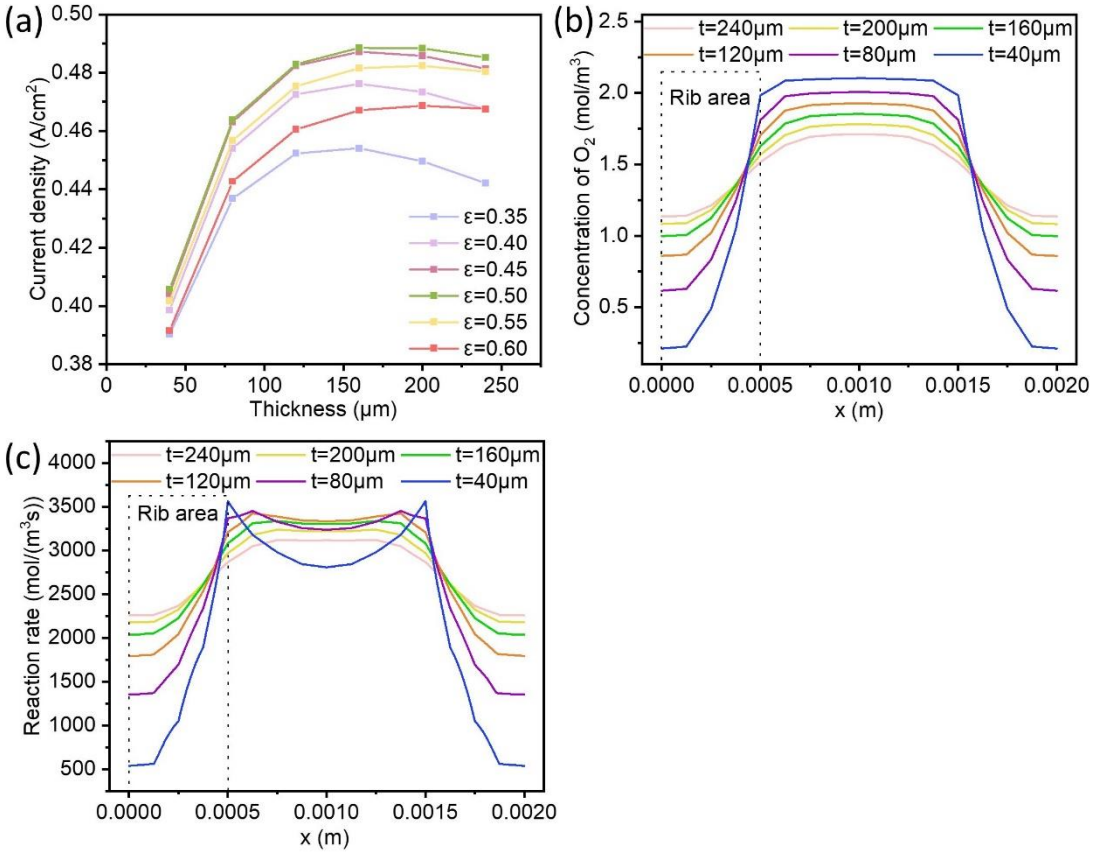

Figure 6 (a) Effects of porosity on current density (b) the O_2 concentration distribution at cathode-electrolyte interface along the x-direction when ε=0.5; (c) the O_2 reaction rate distribution at cathode-electrolyte interface along the x-direction when ε=0.5.

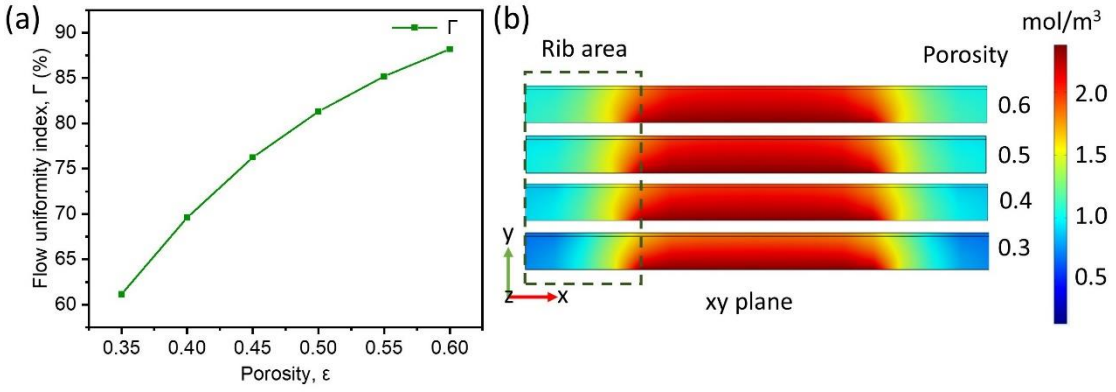

Figure 7 (a) The change of gas uniformity index in the cathode when t=160 μm; (b) the distribution of the oxygen within the cathode when t=160 μm (xy-plane).

Figure 7 (a) shows that the uniformity indicator changes from approximately 61% to approximately 88% when porosity varies from 0.35 to 0.60. In Figure 7 (b), the oxygen is distributed more uniformly within the cathode, especially the region under the rib. Figure 8 (a)

illustrates that the profiles of ohmic loss and concentration loss meet at ε=0.5, where the current density reaches the peak. On the one hand, as shown in Figure 8 (b), the effective electrical conductivity drops with increasing porosity. This can be explained by Eq. (11) which reveals that there is an inverse relationship between effective electrical conductivity and porosity. Thus, the reduction in effective electrical conductivity eventually leads to the increase of ohmic loss. On the other hand, the effective diffusive coefficient grows with the increase of porosity. Based on Eq. (19) and Eq. (20), the effective binary diffusion coefficient and effective Knudsen diffusion coefficient both have a direct relationship with the porosity. Consequently, increasing the cathode porosity is able to reduce the concentration overpotential.

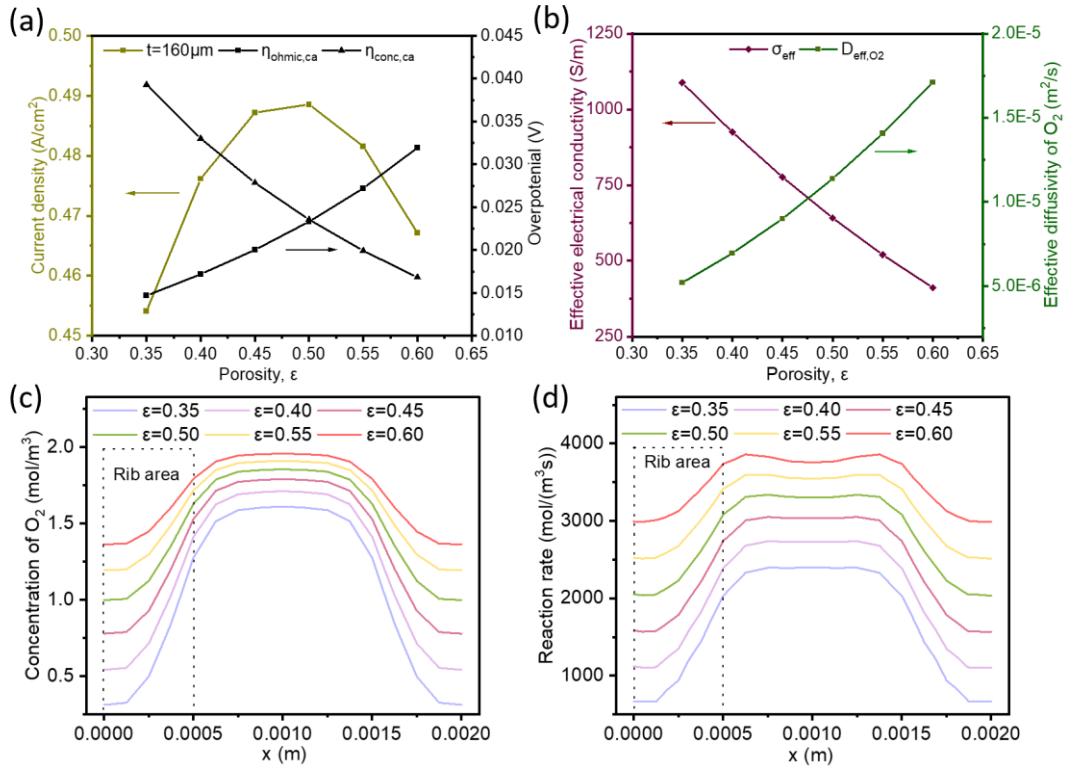

Figure 8 (a) Effects of porosity on current density, ohmic overpotential and concentration overpotential when t=160 μm; (b) effects of porosity on effective electric conductivity and effective diffusion coefficient when t=160 μm; (c) effects of porosity on the O_2 concentration distribution at cathode-electrolyte interface along the x-direction when t=160 μm; (d) effects of porosity on the O_2 reaction rate distribution at cathode-electrolyte interface along the x-direction when t=160 μm.

In Figure 8 (c), the impacts of porosity on the O_2 concentration within the cathode zone

underneath the rib are more considerable than that underneath the channel. However, the difference in concentration between the cathode area underneath the channel and the cathode area underneath the rib becomes smaller. This can be explained by Figure 7 (a), namely, the uniformity of gas flow increases. Figure 8 (d) shows as the porosity grows, the reaction is promoted considerably, while the difference in the reaction rate between the rib-covered cathode and the channel-covered cathode decreases.

3.3 Effects of cathode particle size

The cathode particle size determines the TPB length and the average pore size, which in turn influence the activation loss and the concentration loss of the cathode. As the particle size can be controlled by controlling the fabrication conditions, the effect of particle size on PCFC performance is studied to provide guidance on experimental fabrication process. As mentioned earlier, the electronic and protonic particles are assumed to have the same particle radius. Since electrodes with nanoparticles can be made by a number of methods such as infiltration and in-situ-exsolution [55–58] and several previous modelling studies on the SOFC also consider the nanostructured electrode [34,59,60], this study choose to perform the study on the effects of cathode particle size by varing the particle size from 0.1 μm to 0.6 μm. As shown in Figure 9 (a), the optimal cathode thickness range for PCFC operation also is between 120 μm and 200 μm under various cathode particle radii. Further, the optimal particle radius ranges from 0.2 μm to 0.3 μm. In Figure 9 (b), as the particle radius grows, the TPB length appears an approximately 50% drop while the gas uniformity indicator shows the opposite trend. Since TPBs are generally considered as the place where the electrochemical reactions take place, the reduction in TPB length will lead to an increase in activation loss. In addition, according to Eq. (20), the pore size increases with the rise of particle size as well, thereby leading to the enhancement of Knudsen diffusion and the decrease in the concentration loss eventually. In Figure 9 (b), the blue line shows that the sum of the activation loss and the concentration loss

reaches the bottom when r_s=0.2 μm. Therefore, the optimal particle size is determined by the combined impacts of activation and concentration loss.

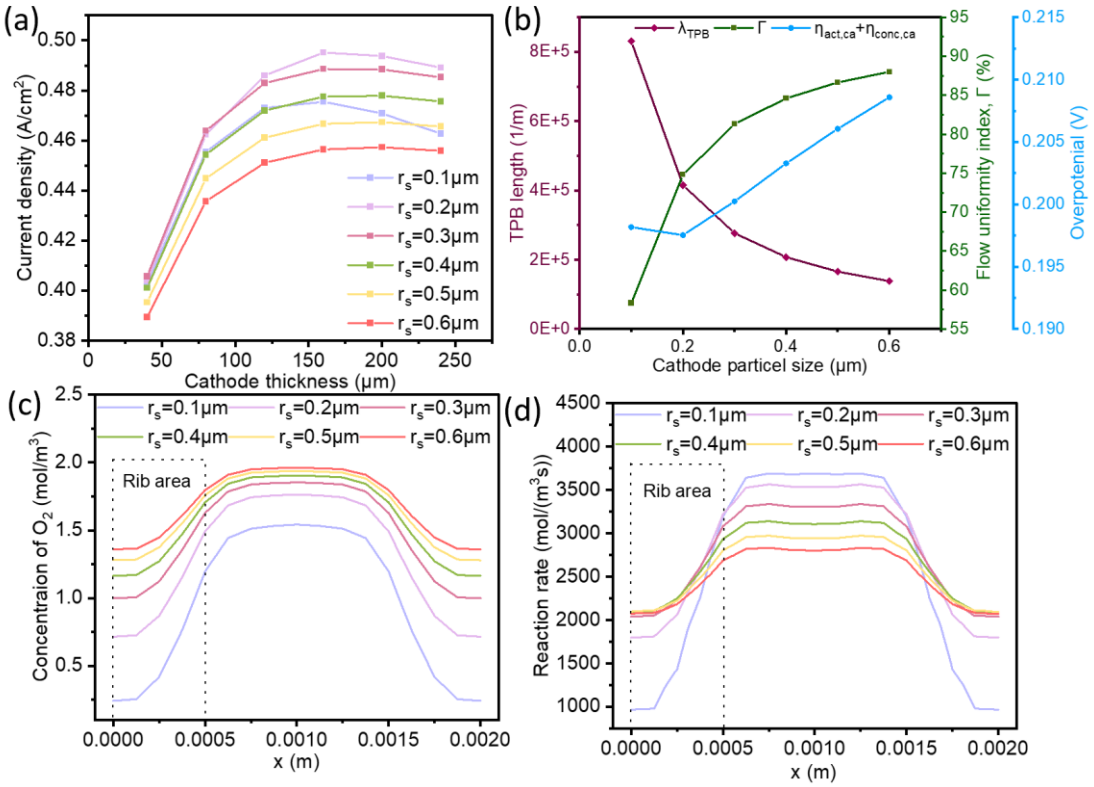

Figure 9 (a) Effects of cathode particle size on current density; (b) effects of cathode particle size on TPB length, gas uniformity indicator and the sum of activation and concentration losses when t =160 μm; (c) effects of cathode particle size on the O_2 concentration distribution at cathode-electrolyte interface along the x-direction when t =160 μm; (d) effects of cathode particle size on the O_2 reaction rate distribution at cathode-electrolyte interface along the x-direction when t =160 μm.

Furthermore, with the rise of particle size, the O_2 concentration within all the areas of the cathode is enhanced (shown in Figure 9 (c)), especially when particle size changes from 0.1 μm to 0.2 μm. As shown in Figure 9 (d), when particle size increases from 0.1 μm to 0.2 μm, a considerable performance augmentation is observed within the cathode region underneath the rib due to the concentration enhancement. However, when the particle size is between 0.3 μm and 0.6 μm, the reaction rates in the half region (away from the channel side) are approximately 2100 mol/(m^3s), while the reaction rates in the rest part (near the channel side) decreases with the increase of particle radius. This observation can be explained by comparing Figure 9 (d)

with Figure 9 (c). When the particle size is between 0.3 μm and 0.6 μm, the O_2 concentration difference in the half region (away from the channel side) is large, where the more TPB sites at the smaller particle size compensate the negative effects on reaction rates caused by the lack of concentration. While the O_2 concentrations of different particle sizes in the rest part (near the channel side) are similar, where the more TPB sites at the smaller particle size lead to higher reaction rates. On the other hand, within the channel-covered cathode area, it suggests that the reaction rate can be weakened by increasing the particle radius owing to the decrease of reaction sites. By comparing the performance of different partitions in the cathode, it can be reasonably concluded that the TPB length is more crucial in the area where the concentration is sufficient. On the contrary, when the reaction sites within the cathode region are abundant, it is more urgent to resolve the concentration limitation issue.

3.4 Effects of electronic phase volume fraction

In order to guarantee the electronic particles are interconnected to form a continuous path for electron conduction, a percolation threshold for the electronic phase volume fraction exists [37]. According to Eq.(12), the percolation probability is a function of the average total coordinate number, particle radius and volume fraction. To maintain the percolation probability between 0 and 1, the range of electronic volume fraction can be calculated from Eq.(12). Thus, the volume fraction is between 0.294 and 0.706. The study on the effects of electronic phase volume fraction is conducted by varying electronic phase volume fraction from 0.3 to 0.7.

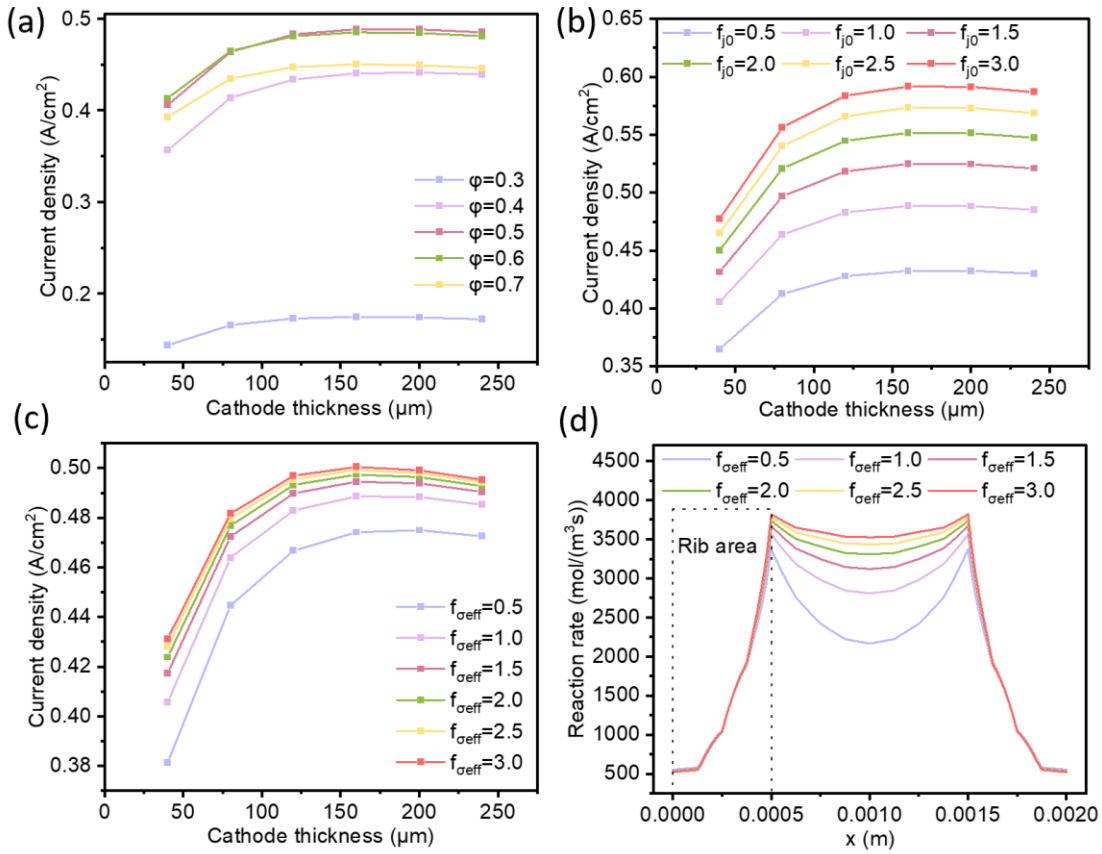

Figure 10 (a) Effects of electronic phase volume fraction on the current density; (b) effects of exchange current density on the current density; (c) effects of effective electric conductivity on the current density; (d) effects of effective electrical conductivity on the O_2 reaction rate distribution at cathode-electrolyte interface along the x-direction when t=40 μm.

Figure 10 (a) shows that the optimal cathode thickness for PCFC operation ranges between 120 μm and 200 μm as well. In addition, when the cathode thickness is less than 100 μm, the optimal volume fraction is 0.6. However, when the cathode thickness is more than 100 μm, the optimal volume fraction is 0.5. Based on Eq. (15), the TPB length also depends on the electronic phase volume fraction. When the particle size ratio is equal to 1, the optimal TPB length cannot be achieved until the volume fraction of the two phases is also the same [37]. Additionally, according to Eq. (11), the addition of electronic phases can lead to an increase in effective electrical conductivity, thereby reducing the ohmic resistance. As discussed in section 3.1, the ohmic loss can be reduced by increasing cathode thickness. Consequently, when the cathode thickness is relatively large (>100 μm), the ohmic loss is not the major performance-limiting

factor, an electronic volume fraction (φ=0.5) with more reaction sites is more desirable. On the contrary, when the cathode thickness is relatively small (<100 μm), more electronic phase (φ=0.6) can reduce the ohmic overpotential.

3.5 Effects of exchange current density and effective electrical conductivity

The exchange current density and effective electric conductivity both are important intrinsic properties of the electrodes. The exchange current density is an indicator of the electrochemical reaction rate. A high exchange current density implies that the electrochemical reaction is easier to proceed. A lower activation overpotential can be obtained, and thus more current can be generated. Therefore, it is important to examine the effects of exchange current density on the PCFC performance. Electrical conductivity is a significant electrode intrinsic property to influence the electron transfer in the PCFC. The ohmic loss can be reduced by increasing electrical conductivity. Hence, it is important to explore the effects of electrical conductivity on the PCFC performance as well as the optimal cathode thickness. In order to conduct the study, two pre-factors (f_{j0} and $f_{\sigma eff}$) are multiplied to the left-hand side of Eq. (7) and Eq. (11) respectively. In each study, the corresponding pre-factor varies from 0.5 to 3.0.

Figure 10 (b) illustrates that the outlines for all values of f_{j0} are similar. The optimal cathode thickness ranges from 120 μm to 200 μm. Although the rise of f_{j0} leads to the increase of current density, its impact on the rate of change of current density is weakened. Another noteworthy finding is that the gain in current density when the thickness is less than 80 μm is smaller than that when the thickness is greater than 80 μm. This phenomenon can lay the blame on the reduction of ohmic loss and the concentration improvement within the rib-covered cathode region.

In Figure 10 (c), the optimal cathode thickness range still situates between 120 μm and 200 μm. The rise of $f_{\sigma eff}$ can enhance the current density, though its impacts on the current density drop

dramatically, indicates that the ohmic overpotential is no longer a performance-limiting factor under high $f_{\sigma eff}$. The limiting factor for PCFC performance is more likely to be either the concentration loss or the sluggish electrochemical reaction in the cathode. In order to gain a more concrete description of the conductivity impacts, Figure 10 (d) shows the reaction rate distribution under various $f_{\sigma eff}$ when t=40 μm. The reaction within the rib-covered cathode area is not changed by $f_{\sigma eff}$, while the reaction within the channel-covered cathode area is considerably promoted. This figure highlights the vital role of ohmic loss in the performance of the cathode area underneath the channel.

4. Conclusions

In this study, a 3D model for an anode-supported PCFC is developed. The percolation theory is incorporated for accounting for the electrode microstructural effects. The modelling results show a good agreement with the experimental data. Different from 1D modelling results suggesting thin cathode, this 3D study demonstrates that the cathode thickness should be controlled in the range between 120 and 200 μm. A too-thin cathode could reduce the average cell performance due to the locally poor performance under the rib, caused by locally low O_2 concentration. This research also demonstrates that the 3D rib effect must be taken into consideration when optimizing the electrode microstructure. The study also shows that for the numerical modelling of single cells, the rib effect must be considered from a three-dimensional perspective when optimizing the electrode microstructure. A comprehensive parametric study is performed on exploring the effects of a series of cathode microstructural properties on the PCFC performance, with full consideration of the rib effect. The complex relationship between cathode microstructural properties and PCFC performance is portrayed thoroughly. This indicates that the cell performance can be improving by carefully controlling the cathode microstructure which directly affects the mass/charge transport and electrochemical reactions processes in the electrode. In addition, the influences of these microstructural parameters on

the optimal cathode thickness are examined as well.

In specific, it is found that the increase in cathode thickness can significantly reduce the ohmic overpotential and enhance the gas distribution, especially the rib-covered cathode. The oxygen depletion region is reduced as well. The cathode porosity plays a pivotal role in balancing the effects of ohmic resistance and concentration overpotential on cell performance. With the increase of porosity, it demonstrates that the concentration loss decreases, while the effective electrical conductivity increases remarkably. The optimal porosity is determined between 0.45 and 0.5. The modelling results on the impacts of cathode particle size illustrate that the TPB length, as well as mass transport, can be directly adjusted by changing the particle size. Consequently, the activation and concentration losses within the porous cathode can be regulated. In contrast, the electronic phase volume fraction affects the electrochemical performance of PCFC by regulating the TPB length and effective electrical conductivity. The optimal electronic phase volume fraction is between 0.5 and 0.6. The investigations on the exchange current density and effective electrical conductivity show that increasing these two properties can improve cell performance, though, its impacts become limited at high values.

The future study can focus on performing the thermal-mechanical analysis of the PCFC cathode since the cathode disruption might be caused by thermal stresses induced by the surging reaction in the cathode region underneath the rib. The effects of the operating parameters on the PCFC performance (working temperature, gas inlet flow rate, working potential) and on the optimal cathode thickness can be also considered in future work. Noteworthy, since PCFC can operate at intermediate temperature (400-600 °C), more experimental data during the PCFC operation, especially operating at low temperature (400 °C), should be collected for future modelling study. Furthermore, more efforts can be devoted to design a novel rib structure, which could be a promising alternative to improve the rib-covered cathode performance as well as eliminate the oxygen depletion region.

Acknowledgments

M. NI thanks the grants (Project Number: PolyU 152064/18E and N_PolyU552/20) from Research Grant Council, University Grants Committee, Hong Kong SAR.

References

[1] Pollitt H. Analysis: Going carbon neutral by 2060 'will make China richer.' Carbon Brief 2020. https://www.carbonbrief.org/analysis-going-carbon-neutral-by-2060-will-make-china-richer (accessed July 21, 2021).

[2] Commission E. Climate strategies & targets 2017:2–3. https://ec.europa.eu/clima/policies/strategies_en (accessed July 25, 2021).

[3] Yu J, Ran R, Zhong Y, Zhou W, Ni M, Shao Z. Advances in porous perovskites: synthesis and electrocatalytic performance in fuel cells and metal-air batteries. Energy & Environmental Materials 2020;3:121–45. https://doi.org/10.1002/eem2.12064.

[4] O'hayre R, Cha S-W, Colella W, Prinz FB. Fuel cell fundamentals. John Wiley & Sons; 2016.

[5] Ormerod RM. Solid oxide fuel cells. Chemical Society Reviews 2003;32:17–28. https://doi.org/10.1039/B105764M.

[6] Beale SB, Andersson M, Boigues-Muñoz C, Frandsen HL, Lin Z, McPhail SJ, et al. Continuum scale modelling and complementary experimentation of solid oxide cells. Progress in Energy and Combustion Science 2021;85:100902. https://doi.org/10.1016/j.pecs.2020.100902.

[7] Fabbri E, Pergolesi D, Traversa E. Materials challenges toward proton-conducting oxide fuel cells: a critical review. Chemical Society Reviews 2010;39:4355–69. https://doi.org/10.1039/B902343G.

[8] Da Silva FS, de Souza TM. Novel materials for solid oxide fuel cell technologies: A literature review. International Journal of Hydrogen Energy 2017;42:26020–36. https://doi.org/10.1016/j.ijhydene.2017.08.105.

[9] Hussain S, Yangping L. Review of solid oxide fuel cell materials: cathode, anode, and electrolyte. Energy Transitions 2020:1–14. https://doi.org/10.1007/s41825-020-00029-8.

[10] Duan C, Tong J, Shang M, Nikodemski S, Sanders M, Ricote S, et al. Readily processed protonic ceramic fuel cells with high performance at low temperatures. Science 2015;349:1321–6. https://doi.org/10.1126/science.aab3987.

[11] Bello IT, Zhai S, Zhao S, Li Z, Yu N, Ni M. Scientometric review of proton-conducting solid oxide fuel cells. International Journal of Hydrogen Energy 2021. https://doi.org/10.1016/j.ijhydene.2021.09.061.

[12] Malik LA, Mahmud NA, Affandi NSM, Mazlan NW, Zakaria NHA, Abd Malek NI, et al. Effect of nickel oxide-Modified BaCe0. 54Zr0. 36Y0. 1O2. 95 as composite anode on the performance of proton-conducting solid oxide fuel cell. International Journal of Hydrogen Energy 2021;46:5963–74. https://doi.org/10.1016/j.ijhydene.2020.10.219.

[13] Mehrpooya M, Khodayari R, Moosavian SMA, Dadak A. Optimal design of molten carbonate fuel cell combined cycle power plant and thermophotovoltaic system. Energy Conversion and Management 2020;221:113177. https://doi.org/10.1016/j.enconman.2020.113177.

[14] Wilailak S, Yang J-H, Heo C-G, Kim K-S, Bang S-K, Seo I-H, et al. Thermo-economic analysis of Phosphoric Acid Fuel-Cell (PAFC) integrated with Organic Ranking Cycle (ORC). Energy 2021;220:119744. https://doi.org/0.1016/j.energy.2020.119744.

[15] Li Z, Zhang H, Xu H, Xuan J. Advancing the multiscale understanding on solid oxide electrolysis cells via modelling approaches: A review. Renewable and Sustainable Energy Reviews 2021;141:110863. https://doi.org/10.1016/j.rser.2021.110863.

[16] Lin B, Wang S, Liu X, Meng G. Stable proton-conducting Ca-doped LaNbO4 thin electrolyte-based protonic ceramic membrane fuel cells by in situ screen printing. Journal of Alloys and Compounds 2009;478:355–7. https://doi.org/10.1016/j.jallcom.2008.11.058.

[17] Bi L, Zhang S, Fang S, Tao Z, Peng R, Liu W. A novel anode supported BaCe0. 7Ta0. 1Y0. 2O3- δ electrolyte membrane for proton-conducting solid oxide fuel cell. Electrochemistry Communications 2008;10:1598–601. https://doi.org/10.1016/j.elecom.2008.08.024.

[18] Yang S, Zhang S, Sun C, Ye X, Wen Z. Lattice incorporation of Cu2+ into the BaCe0. 7Zr0. 1Y0. 1Yb0. 1O3- δ electrolyte on boosting its sintering and proton-conducting abilities for reversible solid oxide cells. ACS Applied Materials \& Interfaces 2018;10:42387–96. https://doi.org/10.1021/acsami.8b15402.

[19] Xie K, Yan R, Chen X, Dong D, Wang S, Liu X, et al. A new stable BaCeO3-based proton conductor for intermediate-temperature solid oxide fuel cells. Journal of Alloys and Compounds 2009;472:551–5. https://doi.org/10.1016/j.jallcom.2008.05.036.

[20] Sun W, Yan L, Shi Z, Zhu Z, Liu W. Fabrication and performance of a proton-conducting solid oxide fuel cell based on a thin BaZr0. 8Y0. 2O3- δ electrolyte membrane. Journal of Power Sources 2010;195:4727–30. https://doi.org/10.1016/j.jpowsour.2010.02.012.

[21] Geisler H, Kromp A, Weber A, Ivers-Tiffée E. Stationary FEM model for performance evaluation of planar solid oxide fuel cells connected by metal interconnectors: I. Model framework and validation. Journal of the Electrochemical Society 2014;161:F778. https://doi.org/10.1149/2.079406jes.

[22] Jeon DH, Nam JH, Kim C-J. Microstructural optimization of anode-supported solid oxide fuel cells by a comprehensive microscale model. Journal of The Electrochemical Society 2006;153:A406. https://doi.org/10.1149/1.2139954.

[23] Liu S, Song C, Lin Z. The effects of the interconnect rib contact resistance on the performance of planar solid oxide fuel cell stack and the rib design optimization. Journal of Power Sources 2008;183:214–25. https://doi.org/10.1016/j.jpowsour.2008.04.054.

[24] Su S, Zhang Q, Gao X, Periasamy V, Kong W. Effects of changes in solid oxide fuel cell electrode thickness on ohmic and concentration polarizations. International Journal of Hydrogen Energy 2016;41:16181–90. https://doi.org/10.1016/j.ijhydene.2016.04.221.

[25] Zhang Y, Zhu A, Guo Y, Wang C, Ni M, Yu H, et al. Electrochemical performance and effect of moisture on Ba0. 5Sr0. 5Sc0. 175Nb0. 025Co0. 8O3-δ oxide as a promising electrode for proton-conducting solid oxide fuel cells. Applied Energy 2019;238:344–50. https://doi.org/10.1016/j.apenergy.2019.01.094.

[26] Xia Y, Jin Z, Wang H, Gong Z, Lv H, Peng R, et al. A novel cobalt-free cathode with triple-conduction for proton-conducting solid oxide fuel cells with unprecedented performance. Journal of Materials Chemistry A 2019;7:16136–48. https://doi.org/10.1039/C9TA02449B.

[27] Xie D, Ling A, Yan D, Jia L, Chi B, Pu J, et al. A comparative study on the composite cathodes with proton conductor and oxygen ion conductor for proton-conducting solid oxide fuel cell. Electrochimica Acta 2020;344:136143. https://doi.org/10.1016/j.electacta.2020.136143.

[28] Yang S, Lu Y, Wang Q, Sun C, Ye X, Wen Z. Effects of porous support microstructure enabled by the carbon microsphere pore former on the performance of proton-

conducting reversible solid oxide cells. International Journal of Hydrogen Energy 2018;43:20050–8. https://doi.org/10.1016/j.ijhydene.2018.09.011.

[29] Lai Y-W, Lee K-R, Yang S-Y, Tseng C-J, Jang S-C, Tsao I-Y, et al. Production of La0. 6Sr0. 4Co0. 2Fe0. 8O3-δ cathode with graded porosity for improving proton-conducting solid oxide fuel cells. Ceramics International 2019;45:22479–85. https://doi.org/10.1016/j.ceramint.2019.07.270.

[30] He F, Song D, Peng R, Meng G, Yang S. Electrode performance and analysis of reversible solid oxide fuel cells with proton conducting electrolyte of BaCe0. 5Zr0. 3Y0. 2O3- δ. Journal of Power Sources 2010;195:3359–64. https://doi.org/10.1016/j.jpowsour.2009.12.079.

[31] Ni M, Leung MKH, Leung DYC. Mathematical modeling of the coupled transport and electrochemical reactions in solid oxide steam electrolyzer for hydrogen production. Electrochimica Acta 2007;52:6707–18. https://doi.org/10.1016/j.electacta.2007.04.084.

[32] Celik AN. Three-dimensional multiphysics model of a planar solid oxide fuel cell using computational fluid dynamics approach. International Journal of Hydrogen Energy 2018;43:19730–48. https://doi.org/10.1016/j.ijhydene.2018.08.212.

[33] Wang Y, Zu B, Zhan R, Du Q, Ni M, Jiao K. Three-dimensional Modeling and Performance Optimization of Proton Conducting Solid Oxide Electrolysis Cell. Fuel Cells 2020;20:701–11. https://doi.org/https://doi.org/10.1002/fuce.201900246.

[34] Kong W, Li J, Liu S, Lin Z. The influence of interconnect ribs on the performance of planar solid oxide fuel cell and formulae for optimal rib sizes. Journal of Power Sources 2012;204:106–15. https://doi.org/10.1016/j.jpowsour.2012.01.041.

[35] Cai Q, Adjiman CS, Brandon NP. Investigation of the active thickness of solid oxide

fuel cell electrodes using a 3D microstructure model. Electrochimica Acta 2011;56:10809–19.

[36] Costamagna P, Costa P, Antonucci V. Micro-modelling of solid oxide fuel cell electrodes. Electrochimica Acta 1998;43:375–94. https://doi.org/10.1016/S0013-4686(97)00063-7.

[37] Chen D, Lin Z, Zhu H, Kee RJ. Percolation theory to predict effective properties of solid oxide fuel-cell composite electrodes. Journal of Power Sources 2009;191:240–52. https://doi.org/10.1016/j.jpowsour.2009.02.051.

[38] Suzuki M, Oshima T. Estimation of the co-ordination number in a multi-component mixture of spheres. Powder Technology 1983;35:159–66. https://doi.org/10.1016/0032-5910(83)87004-1.

[39] Shi J, Xue X. CFD analysis of a symmetrical planar SOFC with heterogeneous electrode properties. Electrochimica Acta 2010;55:5263–73. https://doi.org/10.1016/j.electacta.2010.04.060.

[40] Bouvard D, Lange FF. Relation between percolation and particle coordination in binary powder mixtures. Acta Metallurgica et Materialia 1991;39:3083–90. https://doi.org/10.1016/0956-7151(91)90041-X.

[41] Costamagna P, Panizza M, Cerisola G, Barbucci A. Effect of composition on the performance of cermet electrodes. Experimental and theoretical approach. Electrochimica Acta 2002;47:1079–89. https://doi.org/10.1016/S0013-4686(01)00830-1.

[42] Kong W, Zhu H, Fei Z, Lin Z. A modified dusty gas model in the form of a Fick's model for the prediction of multicomponent mass transport in a solid oxide fuel cell anode.

Journal of Power Sources 2012;206:171–8. https://doi.org/10.1016/j.jpowsour.2012.01.107.

[43] Fuller EN, Schettler PD, Giddings JC. New method for prediction of binary gas-phase diffusion coefficients. Industrial & Engineering Chemistry 1966;58:18–27. https://doi.org/10.1021/ie50677a007.

[44] Brodkey RS, Hershey HC. Transport phenomena: a unified approach. Brodkey publishing; 2003.

[45] Xu H, Chen B, Zhang H, Sun Q, Yang G, Ni M. Modeling of direct carbon solid oxide fuel cells with H2O and CO2 as gasification agents. International Journal of Hydrogen Energy 2017;42:15641–51. https://doi.org/10.1016/j.ijhydene.2017.05.075.

[46] Xu Q, Xia L, He Q, Guo Z, Ni M. Thermo-electrochemical modelling of high temperature methanol-fuelled solid oxide fuel cells. Applied Energy 2021;291:116832. https://doi.org/10.1016/j.apenergy.2021.116832.

[47] Andersson M, Paradis H, Yuan J, Sundén B. Three dimensional modeling of an solid oxide fuel cell coupling charge transfer phenomena with transport processes and heat generation. Electrochimica Acta 2013;109:881–93. https://doi.org/10.1016/j.electacta.2013.08.018.

[48] Todd B, Young JB. Thermodynamic and transport properties of gases for use in solid oxide fuel cell modelling. Journal of Power Sources 2002;110:186–200. https://doi.org/10.1016/S0378-7753(02)00277-X.

[49] Chen B, Xu H, Sun Q, Zhang H, Tan P, Cai W, et al. Syngas/power cogeneration from proton conducting solid oxide fuel cells assisted by dry methane reforming: A thermal-electrochemical modelling study. Energy Conversion and Management 2018;167:37–

44. https://doi.org/10.1016/j.enconman.2018.04.078.

[50] Russner N, Dierickx S, Weber A, Reimert R, Ivers-Tiffée E. Multiphysical modelling of planar solid oxide fuel cell stack layers. Journal of Power Sources 2020;451:227552. https://doi.org/10.1016/j.jpowsour.2019.227552.

[51] Cai B, Song T-F, Su J-R, He H, Liu Y. Comparison of (Pr, Ba, Sr) FeO3-δ-SDC composite cathodes in proton-conducting solid oxide fuel cells. Solid State Ionics 2020;353:115379. https://doi.org/10.1016/j.ssi.2020.115379.

[52] Hou J, Dong K, Miao L, Liu W. Rationally structuring proton-conducting solid oxide fuel cell anode with Ni metal catalyst and porous skeleton. Ceramics International 2020;46:24038–44. https://doi.org/10.1016/j.ceramint.2020.06.181.

[53] Huang CM, Shy SS, Lee CH. On flow uniformity in various interconnects and its influence to cell performance of planar SOFC. Journal of Power Sources 2008;183:205–13. https://doi.org/10.1016/j.jpowsour.2008.04.059.

[54] Wu X, Yang D, Wang J, Li X. Temperature gradient control of a solid oxide fuel cell stack. Journal of Power Sources 2019;414:345–53. https://doi.org/10.1016/j.jpowsour.2018.12.058.

[55] Yang X, Sun W, Ma M, Xu C, Ren R, Qiao J, et al. Enhancing Stability and Catalytic Activity by In Situ Exsolution for High-Performance Direct Hydrocarbon Solid Oxide Fuel Cell Anodes. Industrial \& Engineering Chemistry Research 2021. https://doi.org/10.1021/acs.iecr.1c00806.

[56] Lee JJ, Kim K, Kim KJ, Kim HJ, Lee YM, Shin TH, et al. In-situ exsolution of Ni nanoparticles to achieve an active and stable solid oxide fuel cell anode catalyst on A-site deficient La0. 4Sr0. 4Ti0. 94Ni0. 06O3-δ. Journal of Industrial and Engineering

Chemistry 2021;103:264–74. https://doi.org/10.1016/j.jiec.2021.07.037.

[57] Ozmen O, Lee S, Hackett G, Abernathy H, Zondlo JW, Sabolsky EM. Efficient and controlled nano-catalyst solid-oxide fuel cell electrode infiltration with poly-norepinephrine surface modification. Journal of Power Sources 2021;485:229232. https://doi.org/10.1016/j.jpowsour.2020.229232.

[58] Shaheen K, Shah Z, Gulab H, Hanif MB, Faisal S, Suo H. Metal oxide nanocomposites as anode and cathode for low temperature solid oxide fuel cell. Solid State Sciences 2020;102:106162. https://doi.org/10.1016/j.solidstatesciences.2020.106162.

[59] Chan SH, Chen XJ, Khor KA. Cathode micromodel of solid oxide fuel cell. Journal of the Electrochemical Society 2003;151:A164.

[60] Menon V, Fu Q, Janardhanan VM, Deutschmann O. A model-based understanding of solid-oxide electrolysis cells (SOECs) for syngas production by H2O/CO2 co-electrolysis. Journal of Power Sources 2015;274:768–81. https://doi.org/https://doi.org/10.1016/j.jpowsour.2014.09.158.